# First-principles investigation of V-doping effects on Fe3Cr4C3 carbide in hypereutectic Fe–Cr–C hardfacing Coating

**Zhijun Shi[a], Wei Shao[a], Xiaolei Xing[a,b], Xuejun Ren[c], Yefei Zhou[a,b]* and Qingxiang Yang[a]***

[a]State Key Laboratory of Metastable Materials Science and Technology, Yanshan University, Qinhuangdao 066004, People's Republic of China,

[b]College of Mechanical Engineering, Yanshan University, Qinhuangdao 066004, People's Republic of China,

[c]School of Engineering, Liverpool John Moores University, Liverpool L3 3AF, United Kingdom.

*Correspondence e-mail: yfzhou@ysu.edu.cn, qxyang@ysu.edu.cn

**Abstract:**

The mechanical property improvement of M7C3 carbides in hypereutectic Fe–Cr–C hardfacing coating is required for its widespread application and longer service life. Vanadium is a frequently used alloying element, while the effects of V doping on the stability and tensile properties of M7C3 carbide have been rarely reported. In this article, the formation enthalpy, structural stability, anisotropic tensile properties and electronic structure of V-doped M7C3 (Fe3Cr4C3) carbide were calculated by the first-principles method. The mechanism by which the tensile property of Fe3Cr4C3 carbide can be improved by V-atom doping is discussed. The results show that the formation enthalpy (-0.24 eV/atom) of Fe3Cr3VC3 carbide is lower than that (0.48 eV/atom) of Fe3Cr4C3 carbide, which indicates that the formation of Fe3Cr3VC3 carbide is more facile. The absence of an imaginary frequency in the phonon dispersion spectra reveals that the Fe3Cr3VC3 carbide model is stable. Compared with Fe3Cr4C3 carbide, the tensile strength of Fe3Cr3VC3 carbide in the (0001) crystal face is increased from 44.42 to 48.46 GPa and that in the (1111) crystal face is also increased, from 28.99 to 34.19 GPa. The reasons that the tensile property of Fe3Cr4C3 can be improved by V doping are the electron redistribution and thenformation of stronger bonds in Fe3Cr3VC3 carbide.

## 1. Introduction

Hypereutectic Fe–Cr–C hardfacing coatings, which not only have excellent toughness, high thermal conductivity and good thermal stability like metals, but also have the characteristics of high temperature, corrosion and wear resistance like ceramics, have been widely applied in the additive manufacturing and wear resistance industrial fields (Li et al., 2009, 2019; Yılmaz & Turhan, 2001). In hypereutectic Fe–Cr–C hardfacing coatings, M7C3 (M = Fe, Cr) carbide is the main strengthening phase due to its high hardness and excellent wear resistance (Buchanan et al., 2007). With the rapid development of additive manufacturing, there is an increasing requirement for improving the strength ofa M7C3 carbide so as to further enhance the mechanical properties of hypereutectic Fe–Cr–C hardfacing coatings (Rahman et al., 2019). Therefore, it is significant to control and optimize the properties of M7C3 carbide to improve the performance and wear resistance of hypereutectic Fe–Cr–C hardfacing coatings (Wiengmoon et al., 2005; Khvan et al., 2014; Zhi et al., 2008).

The performance of materials can be effectively adjusted and controlled by adding alloying elements, in which respect the transition-metal element V has attracted widespread attention (Yin et al., 2020). Bedolla-Jacuinde (2001) demonstrated that V (1.98%) can dissolve in M7C3 carbide to increase its volume fraction and hardness. Lu et al. (2008) studied the effects of V doping on the microstructure and soft magnetic properties of Finemet-type alloys, which reveals that the grain size is further refined with the increase of Vaddition and its magnetic properties

are also improved. Fan et al. (2020) studied the structure and piezoelectric properties of V-doped ZnO thin films and the results show that as the annealing temperature or time increases, the degree of the c-axis preferred orientation and grain size are increased, improving the piezoelectric performance. Vanadium is a frequently used alloying element. However, the effects of V doping on the stability and tensile properties of M7C3 carbide have been rarely reported. Meanwhile, it is difficult and incomplete to explain its mechanism by experiment.

In recent years, first-principles methods based on density functional theory (DFT) have attracted increasing attention and been widely used in research on material properties and micro-mechanism (Lu et al., 2021; Wei et al., 2020; Liao et al.,2020). Rogl et al. (2017) investigated the effects of V and Nb doping on the thermoelectric and mechanical properties of half-Heusler alloys based on {Ti, Zr, Hf}NiSn by experimental and DFT calculation methods. The results showed that all the mechanical properties, including hardness, elastic modulus, cracking resistance and fracture toughness, of the samples are improved by Vand Nb dopants. Liao et al. (2018, 2020) studied the effects of transition-metal elements on the phase stability, elastic properties and thermodynamic properties of Nb–Ti–V–Zr high-entropy alloys by virtual crystal approximation (VCA) and the first-principles method, which indicated that the Nb and V additives increase the stability of the bodycentred cubic (bcc) structure, while Ti and Zr additives decrease its stability. Moreover, Nb and Ti additives have remarkable effects on density, while their effect on lattice constants are slight as opposed to V and Zr additives. In addition, they also revealed that Nb and V additives have a positive influence on Young's modulus, shear modulus and isotropy properties, while Ti and Zr additives present the opposite effect. Miao et al. (2020) studied the electronic structure and magnetism performance of the V-doped monolayer MoS2 and found that as the tensile strain is increased, the double exchange between V and Mo atoms is reduced, resulting in a lowered spin polarization in V-doped MoS2. Among the hypereutectic Fe–Cr–C hardfacing coatings, M7C3 carbide is a type of mixed carbide with strong anisotropy (Chong et al., 2019) and its mechanical properties are influenced by the Cr/Fe ratio (Guo et al., 2021). Zhang et al. (2013) studied the stability and mechanical properties of hexagonal Fe7–xCrxC3 with a different Fe/Cr ratio by the first principles method and found that Fe3Cr4C3 was more stable than other structures. Therefore, Fe3Cr4C3 carbide is usually used to approximate the atomic structure of M7C3 carbide in theoretical calculations.

In the present work, the formation enthalpy, phonon dispersion spectrum and heat capacity of Fe3Cr4C3 and Fe3Cr3VC3 carbides were calculated via a first-principles method to evaluate the thermodynamic and dynamic stability of Fe3Cr3VC3 carbide. The tensile properties of Fe3Cr4C3 and Fe3Cr3VC3 carbides in different crystal faces were then calculated and comparatively analyzed. Finally, the electronic structures and bond characteristics of Fe3Cr4C3 and Fe3Cr3VC3 carbides were calculated to explain the mechanism by which the tensile properties of Fe3Cr4C3 can be improved by V doping. This work can provide a theoretical basis for the design and development of novel V-doped Fe3Cr4C3 carbide to reinforce wear-resistant coatings.

## 2. Calculation details

The first-principles calculation processes were performed with the Vienna Ab initio Simulation Package (VASP), first-principles computing software based on the DFT framework (Kresse & Furthmuller, 1996). The general gradient approximation (GGA) parameterized by Perdew–Burke–Ernzerhof (PBE) was used to deal with the exchange correlation function of pseudopotential (Perdew et al., 1996). The interactions between nuclei and valence electrons was handled with the PAW method (Blochl, 1994). Based on the convergence tests, the cutoff

energy was set at 500 eV with selected electron orbits: C s2p2, Cr d5s1, Fe d7s1 and V p6d4s1. The K-point grids (Kang et al., 2011) sampled in the Brillouin region were set at 8 x 8 x 8 and the Monkhorst–Pack scheme was used to extend the construction. When energy changes between two successive steps were lower than $10^{-6}$ eV and the absolute values of the ionic force changes were lower than $10^{-4}$ eVÅ$^{-1}$, it can be recognized that the electronic structures were convergent. From the calculations of different cell sizes (Figs. S2 and Table S1), considered with respect to the accuracy of the interatomic force calculations and the consumption of computing resources, the 2x 2x2 supercell was large enough for phonon dispersion spectrum calculations. The tensile properties were calculated by the ideal strength method (Zhang et al., 2014; Roundy et al., 1999; Li et al., 2015). The VASP code was modified to perform the x-axis fixed optimization. In the primary model, lattice 'a' is along the x axis and lattice 'c' is along the z axis, which is applied in the [2110] direction tensile calculation. For tensile calculation in the [0001] direction, the rotation angle of the crystal cell around the y axis is 90°. For the tensile calculation in the [1120] direction, the rotation angle of the crystal cell around the z axis is 60°. For the tensile calculation in the [1121] direction, the rotation angle of the crystal cell along the z axis is 60°, and those along the y axis in Fe3Cr4C3 and Fe3Cr3VC3 carbides are 31.41 and 31.36°, respectively. The strain step was set at 0.01. For the magnetic interactions in the calculations, the structural energies of Fe3Cr3VC3 with and without spin polarization were calculated, and the values are -182.18 and -182.02 eV, respectively. The difference between them is 0.16 eV (0.09%). Therefore, the magnetic influence was not taken into account in this work.

## 3. Results and analysis

### 3.1. Crystal structures and stability of V-doped Fe3Cr4C3 carbide

Similar to Fe7C3 carbide, the crystal structure of Fe3Cr4C3 carbide also belongs to the hexagonal system, with the space group P63mc (Xie et al., 2005). There are two kinds of Wyckoff sites (6c and 2b) in the Fe3Cr4C3 carbide model, in which six C atoms, six Fe atoms and six Cr atoms are at Wyckoff 6c sites, and the other two Cr atoms are atWyckoff 2b sites (Table S2). In particular, the fractional coordinates of two Wyckoff 2b sites occupied by V atoms in the following calculations are (0.3333, 0.6667, 0.818) and (0.6667, 0.3333, 0.318). It is known that formation enthalpy is usually used to judge the stability of doping systems (Gao et al., 2014). The schematic structures and formation enthalpy calculations of Fe3Cr4C3 and multicomponent FexCr6.5–xV0.5C3 carbides are shown in Fig. 1. In the unit-cell structures of Fe3Cr4C3 and multicomponent FexCr6.5–xV0.5C3 carbides, the blue spheres are Cr atoms, the yellow spheres are Fe atoms, the red spheres are Vatoms and the small brown spheres are C atoms. The formation enthalpy Hf was calculated at 0 K and 105 Pa. The equation (Gao et al., 2014) is shown as follows:

$$H_{\mathrm{f}} = \frac{1}{\sum N_i}\left[E_{\mathrm{total}} - \sum(N_i E_i)\right] \qquad (1)$$

where Etotal is the enthalpy of the carbide unit cells, Ei is the enthalpy of different atoms in the carbide models and Ni is the number of different atoms. In Fig. 1, the structural formation enthalpy of Fe3Cr4C3 carbide with V atoms doped in the Wyckoff 2b sites is the lowest, which indicates that it is the easiest way to form stable V-doped Fe3Cr4C3 carbide. Research shows that Fe3Cr4C3 carbides with doping atoms in the Wyckoff 2b sites are preferably formed (Chong et al., 2019). The calculated Hf of Fe3Cr4C3 carbide is 0.48 eV/atom and that of Fe3Cr3VC3 carbide is decreased to _0.24 eV/atom, which indicates that Fe3Cr3VC3 carbide is more stable and easier to be formed at 0 K and 105 Pa than Fe3Cr4C3 carbide. From

structures with V atoms in the Wyckoff 2b sites, the total enthalpies of Fe3Cr3.5V0.5C3 and Fe3Cr3VC3 are _182.028 and _182.019 eV, respectively. The difference is very small, i.e. 0.009 eV (about 0.005%). The formation enthalpy of Fe3Cr3.5V0.5C3 is about -0.2475 eV/atom, which is lower than that of Fe3Cr3VC3 and so is much easier to form from a purely energetic point of view. But Fe3Cr3.5V0.5C3 seems to violate the symmetry operations, with only one Wyckoff 2b atom replaced by a V atom. In Fig. S3, the difference of the electron distributions between different atoms in Wyckoff 2b sites can be seen clearly, which can contribute to the consequential increase of the anisotropy in the bonding characteristics and mechanical properties. Therefore, Fe3Cr3VC3 is more mechanically stable and crystallographically reasonable than Fe3Cr3.5V0.5C3.

The unit cell and polyhedral structure of Fe3Cr3VC3 carbide are shown in Fig. 2. After geometric optimization, the lattice constants of Fe3Cr4C3 carbide are a = 6.98 and c = 4.26 Å , and its volume (V) is 180.42 $Å^3$, which is close to the experimental (Chong et al., 2019) and computational (Zhang et al., 2013) results, viz. a = 6.99, c = 4.27 Å and V = 181.08 $Å^3$. After V atoms are doped in the Wyckoff 2b sites, lattice distortion appears in Fe3Cr3VC3 carbide and the lattice constants are increased to a = 7.04 and c = 4.28 Å , and the volume is increased to 184.12 $Å^3$. Although lattice distortion exists in Fe3Cr3VC3 carbide, its thermodynamic stability is greater than that of Fe3Cr4C3 carbide. The phonon dispersion spectrum can be used to investigate the dynamic stability of Fe3Cr4C3 and Fe3Cr3VC3 carbides. The phonon dispersion spectra and phonon density of states (PHDOS) of Fe3Cr4C3 and Fe3Cr3VC3 carbides are shown in Fig. 3. There are no imaginary frequencies in the phonon dispersion spectra, which indicates that the Fe3Cr4C3 and Fe3Cr3VC3 crystal models are theoretically stable. It is obvious that the high-frequency parts of the PHDOS are mainly contributions of C-atom vibrations and the low-frequency parts are contributed by metal atoms. The major PHDOS peaks of the V atoms are in the range from 150 to 350 cm_1, in which the PHDOS peaks of the Cr and Fe atoms are weakened by V doping. However, the effects of V doping on the high-frequency parts (optical branches in the phonon spectrum) are negligible. Therefore, the V doping atoms have some effect on the thermodynamic properties and do not obviously affect the optical properties. The thermodynamic properties determined on the basis of phonon spectrum calculations are shown in Fig. 4, which can reflect thermodynamic stability. Fig. 4(a) shows the enthalpy, free energy and entropy curves with temperature of Fe3Cr4C3 and Fe3Cr3VC3 carbides. The solid and dashed lines distinguish the curves of the Fe3Cr4C3 and Fe3Cr3VC3 carbides. With increasing temperature, the free energy decreases, while enthalpy and entropy increase. In addition, the slightly lower free energy of Fe3Cr3VC3 carbide reveals that it is more stable than Fe3Cr4C3 carbide. Fig. 4(b) shows the Debye temperature curves of the Fe3Cr4C3 and Fe3Cr3VC3 carbides. The Debye temperature increases with increasing temperature (starting from 0 K). When the temperature is below 720 K, the Debye temperature of Fe3Cr4C3 carbide is greater than that of Fe3Cr3VC3 carbide. When the temperature is above 720 K, the Debye temperature of Fe3Cr4C3 carbide is lower than that of Fe3Cr3VC3 carbide. In particular, the Debye temperature changes rapidly when the temperature is below 400 K, which corresponds with the sharp range of change of heat capacity shown in Fig. 4(c). The heat capacity of Fe3Cr3-VC3 carbide is slightly larger than that of Fe3Cr4C3 carbide in the low-temperature range from 50 to 350 K and its heat capacity will follow quantum rules when the temperature is much lower than the Debye temperature. When the temperature is above 720 K, the heat capacity approaches a constant value, which will follow the Dulong–Petit rule (Petit & Dulong, 1819).

3.2. Atomic tensile properties of Fe3Cr4C3 and Fe3Cr3VC3 carbides

The diagrams of selected tensile crystal faces in Fe3Cr3VC3 carbide are shown in Fig. 5 to help understand the crystal tensile directions. Fig. 5(a) shows the locations and relationship of the selected crystal faces for tensile calculation, in which the red plane represents the (0001) crystal face, the yellow plane represents the (2110) crystal face, the green plane represents the (1120) crystal face and the blue plane represents the (1121) crystal face. Fig. 5(b) shows the schematic locations of the (0001) and (2110) crystal faces in the Fe3Cr3VC3 carbide 2 x 2 x 2 supercell. Fig. 5(c) shows the locations of the (1120) crystal face in the Fe3Cr3VC3 carbide 2x2 x2 supercell. Fig. 5(d) shows the location of the (1121) crystal face in the Fe3Cr3VC3 carbide 2x2x2 supercell.

The tensile properties of Fe3Cr4C3 and Fe3Cr3VC3 carbides in different crystal faces are shown in Fig. 6 (data in Table S3). Fig. 6(a) shows the tensile stress–strain curves of Fe3Cr4C3 and Fe3Cr3VC3 carbides in the (0001), (2110), (1120) and (1121) crystal faces, in which T0 is the point corresponding to the initial structure, T1 is the highest point of the stress–strain curve, which represents the ideal tensile strength of the carbide structure, and T2 is the point corresponding to the tensile fracture structure. In the uniaxial tensile calculation process, fracture was defined at the position of the breaking of the chemical bonds, which is shown as a sudden change in the stress–strain curve. In ab initio calculations, the structural energy changes when chemical bonds are fractured. Therefore, the fracture can be recognized as a sudden change in the stress–strain curve calculated by the following equation:

$$\sigma = \frac{(1+\varepsilon)}{V(\varepsilon)}\frac{\partial E}{\partial \varepsilon} \qquad (2)$$

where σ is the uniaxial tensile stress, E is the structural energy of the system corresponding to the tensile strain ε at each step and V(ε) is the structural volume under the corresponding strain.

The critical strain of a single unit cell after tensile fracture was defined as the fracture elongation δ, which can be calculated by the following equation:

$$\delta = \frac{L - L_0}{L_0} \qquad (3)$$

where L is the tensile directional length of the unit cell after fracture and L0 is the tensile directional length of the initial unit cell.

The tensile strengths and fracture elongations of Fe3Cr4C3 and Fe3Cr3VC3 carbides in different crystal faces are summarized in Fig. 6(b). The tensile strengths of Fe3Cr4C3 and Fe3Cr3VC3 carbides in the (2110) crystal face are 25.74 and 20.61 GPa, respectively, which indicate that the tensile strength of Fe3Cr3VC3 carbide in the (2110) crystal face is 5.13 GPa lower than that of Fe3Cr4C3 carbide. The tensile strengths of Fe3Cr4C3 and Fe3Cr3VC3 carbides in the (1120) crystal face are 26.47 and 20.24 GPa, respectively, which indicate that the tensile strength of Fe3Cr3VC3 carbide in the (1120) crystal face is 6.23 GPa lower than that of Fe3Cr4C3 carbide. However, the tensile strengths of Fe3Cr4C3 and Fe3Cr3VC3 carbides in the (0001) crystal face are 44.42 and 48.46 GPa, respectively, which indicate that the tensile strength of Fe3Cr3VC3 carbide is 4.04 GPa greater than that of Fe3Cr4C3 carbide. The tensile strengths of Fe3Cr4C3 and Fe3Cr3VC3 carbides in the (1121) crystal face are 28.99 and 34.19 GPa, respectively, which indicate that the tensile strength of Fe3Cr3VC3 carbide is 5.2 GPa greater than that of Fe3Cr4C3 carbide. There is no significant changes for the δ value of

Fe3Cr3VC3 and Fe3Cr4C3 carbides in the (2110) and (1120) crystal faces, and the δ values are all 7%. The δ value of Fe3Cr4C3 carbide in the (0001) crystal face is 36% and that of Fe3Cr3VC3 carbide in the (0001) crystal face is 31%, which indicates that the δ value of Fe3Cr3VC3 carbide in the (0001) crystal face is 5% smaller than that of Fe3Cr4C3 carbide. The δ value of Fe3Cr4C3 carbide in the (1121) crystal face is 30% and that of Fe3Cr3VC3 carbide in the (1121) crystal face is 29%, which indicates that the δ value of Fe3Cr3VC3 carbide in the (1121) crystal face is 1% smaller than that of Fe3Cr4C3 carbide.

It is known that the excellent wear resistance of Fe3Cr4C3 carbide is mainly contributed by its (0001) face, and the 1/3 [2110] edge dislocation glides along the (0001) plane are the most likely contribution to its strain and deformation ability (Wang et al., 2016). Therefore, the increase in ideal strength of Fe3Cr3VC3 carbide in the (0001) and (1121) crystal faces can be beneficial to the wear resistance improvement of the Fe–Cr–C hardfacing coating and the slight decreases of δ values are acceptable. The decreases of ideal strength in the (2110) and (1120) crystal faces have no significant influence on the δ value or the deformation ability.

The atomic scale tensile simulation could be seen as the tensile process of chemical bonds (Zhang et al., 2015). The bond lengths in Fe3Cr4C3 and Fe3Cr3VC3 carbides are collected and shown in Fig. 7, in which the blue hollow square represents different bond lengths in Fe3Cr4C3 and the red hollow triangle represents different bond lengths in Fe3Cr3VC3 carbide. In Fig. 7(a), the C—Cr, C—Fe, Cr—Fe, Fe—Fe and Cr—Cr bond lengths range from 1.99 to 2.76 Å . The C—V, V—Fe and Cr—V bonds are added in Fe3Cr3VC3 carbide relative to Fe3Cr4C3 carbide and the bond lengths also range from 1.99 to 2.76 Å. In Fig. 7(a2), the bond lengths are increased with a 10% tensile strain, in which the bond-length increase of the Cr—Fe bond in Fe3Cr4C3 carbide is the largest and is close to 2.98 Å. As the tensile deformation is further increased to 20%, the Cr—Fe bond length changes of Fe3Cr3VC3 carbide in Fig. 7(a3) are relatively larger than those of Fe3Cr4C3 carbide. In Fig. 7(a4), the bond-length differences in Fe3Cr4C3 and Fe3Cr3VC3 carbides are increased rapidly and their bond-length distributions become disordered. By comparing Figs. 7(b) and 7(c), as well as Figs. 7(b2) and 7(c2), Figs. 7(b3) and 7(c3), and Figs. 7(b4) and 7(c4), it can be seen that the bond-length changes of Fe3Cr4C3 and Fe3Cr3VC3 carbides in the (2110) and (1120) crystal faces are distributed in a similar manner. This can explain the similar tensile behaviors of Fe3Cr4C3 and Fe3Cr3VC3 carbides in the (2110) and (1120) crystal faces. The bond-length distribution of the 0% strain (2110) and (1120) crystal faces ranges from 1.91 to 2.72 Å. With the increase of tensile strain, the bond-length change increases and that of the Cr—Cr bond in Fe3Cr4C3 carbide becomes dominant, with a 3.01 Å bond length. In the fracture structures with 7% strain, the Cr—Cr bond length of Fe3Cr4C3 and Fe3Cr3VC3 carbides in the (2110) and (1120) crystal faces is the largest, with a value of 3.05 Å. In Fig. 7(d), the bond-length distribution of Fe3Cr4C3 and Fe3Cr3VC3 carbides in the (1121) crystal face is consistent with those in the (0001), (2110) and (1120) crystal faces, as shown in Figs. 7(a), 7(b) and 7(c). When the strain is increased to 10%, the degree of bond-length distribution disorder in Fig. 7(d2) is also increased, in which the Cr—Fe bond-length maximum is 2.97 Å. Nevertheless, when the strain is further increased to 20%, the Cr—Cr bond lengths of Fe3Cr3VC3 carbide in Fig. 7(d3) are obviously changed and the maximum is 3.07 Å. In the fracture structures shown in Fig. 7(d4), the Cr—Fe bond lengths of Fe3Cr4C3 carbide are further increased and the maximum approaches 3.12 Å. It is worth noting that the degree of bond-length disorder in the (0001) crystal faces changes most rapidly with the strain increase from 0 to 30/36%. For a deeper investigation of the mechanism, the electronic structures may have a decisive influence on the tensile behaviors.

## 4. Discussion

### 4.1. Electronic structures of Fe3Cr4C3 and Fe3Cr3VC3 carbides

The Electron Localization Function (ELF) (Becke &Edgecombe, 1990) can be used to qualitatively characterize the localized distribution feature of electrons and assist in verifying bond types. The ELF equation is as follows:

$$ELF = 1/\left[1 + \left(\frac{D_{(r)}}{Dh_{(r)}}\right)^2\right], \qquad (4)$$

where D(r) is the real electron density and Dh(r) is the uniform electron gas density. ELF values vary from 0 to 1. When ELF = 1 the electrons are completely localized, when ELF=0.5 the electrons are in a uniform electron gas state and when ELF = 0 the electrons are completely delocalized (or there are no electrons).

The electronic structures of Fe3Cr4C3 and Fe3Cr3VC3 carbides in the different crystal faces are shown in Fig. 8. Fig. 8(a) shows ELF planar projections of Fe3Cr4C3 carbide in the (0001), (2110), (1120) and (1121) planes. There are large electron delocalization regions with ELF = 0 around the Cr atoms and relatively smaller ones around the Fe atoms. The atomic gain and loss of electrons agrees with the law of Pauling electronegativity (C 2.55 > Fe 1.83 > Cr 1.66). There are electron localization regions with the ELF ranging from 0.7 to 0.8 around C atoms. These indicate that C—Cr and C—Fe are polar covalent bonds. In the (0001) plane, the trigeminal region with the ELF ranging from 0.3 to 0.5 between three Fe atoms and three Cr atoms indicates that the bond type of Fe—Cr is a metallic bond. There are regions with ELF = 0.5 between metal atoms in the (2110), (1120) and (1121) planes, which also indicates the formation of metallic bonds. Fig. 8(b) shows ELF planar projections of Fe3Cr3VC3 carbide in the (0001), (2110), (1120) and (1121) planes. Similar to Fe3Cr4C3 carbide, there are large electron delocalization regions with ELF = 0 around the metal atoms in Fe3Cr3VC3. The action of the V atom is similar to that of the Cr atom due to their similar Pauling electronegativity (Cr 1.66 and V 1.63). In the (0001) plane of Fe3Cr3VC3 carbide, the area of the trigeminal region with ELF = 0.5 is larger than that of Fe3Cr4C3 carbide, which reveals that stronger metallic bonds can be formed. The areas of the regions with ELF = 0.5 in the (0001), (2110), (1120) and (1121) planes are increased, as is the bond strength. The electron localization ELF values around the C atoms in the C—V bonds are larger than those of the C—Cr bonds, which reveals that the strength of the C—V bond is larger than that of the C—Cr bond. Therefore, the electron redistribution caused by V doping can lead to the formation of stronger chemical bonds, and the mechanical properties are then improved. The decrease of tensile strength in the (2110) and (1120) crystal faces are attributed to the relatively larger lattice distortions in their tensile orientations, which could lead to greater bond lengths and lower bond strengths.

A semi-quantitative analysis of electron transfer can be made by Bader charge calculations, as shown in Fig. 9. The Bader charges of atoms in Fe3Cr4C3 and Fe3Cr3VC3 carbides are shown in Figs. 9(a) and 9(b). Those of atoms in the C, Cr,Fe and V crystal models are shown in Figs. 9(c), 9(d), 9(e) and 9(f); the values are 4, 6, 8 and 5, respectively. In the Fe3Cr4C3 carbide model, the Bader charge values of the C, Cr and Fe atoms are about 5.15, 5.30 and 7.78, respectively. After V doping, The Bader charge values of the C, Cr and Fe atoms are increased to about 5.18, 5.31 and 7.83, respectively, which reveals that the Fe and Cr atoms lose fewer electrons and the C atoms gain more electrons. In the Fe3Cr3VC3 carbide model, the Bader charge value of the V atom is about 4.08 and its electronic loss quantity is approximatively 1 electron per atom. Electron depletion of the V atom is stronger than other metallic atoms and this can lead to electron redistribution. Band structures and density of states (DOS) of the Fe3Cr4C3 and Fe3Cr3VC3 carbide models are shown in Fig. 10, in which the position of the

Fermi level is at 0 eV. Fig. 10(a) shows the band structures of Fe3Cr4C3 carbide. The bands are mainly accumulated around the Fermi level (from -7.5 to 5 eV) and this shows very strong bonding reactions. There are several bands across the Fermi level, which indicates that there are some metallic characteristics in Fe3Cr4C3 carbide. Fig. 10(b) shows the band structures of Fe3Cr3VC3 carbide. There are little differences between the band structures of the Fe3Cr4C3 and Fe3Cr3VC3 carbide models. The major part of the band structures of Fe3Cr3VC3 also range from -7.5 to 5 eV. There are some changes of the band structures around 15 eV in Fe3Cr3VC3 carbide. Due to the similar Pauling electronegativities between V and Cr atoms and the small addition of V dopant, the effects on the band structures and DOS are relatively small.

This can also be proved by the total density of states (TDOS) and partial density of states (PDOS), as shown in Fig. 10(c). The curves with different colours are the TDOS and PDOS of Fe3Cr4C3 carbide, while those of Fe3Cr3VC3 carbide are represented by shadowed regions. The Fermi level is indicated by the dotted line. Compared with Fe3Cr4C3 carbide, the right shift and slight reduction of the TDOS peaks of Fe3Cr3VC3 carbide can be seen clearly. The PDOS peaks of C-p orbitals are distributed on both sides of the Fermi level and its right shift can contribute to a larger pseudogap, which indicates that the covalent bonds between C atoms and other metal atoms in Fe3Cr3VC3 carbide are enhanced. The PDOS of Fe-d orbitals, as well as those of Cr-d and V-d orbitals, have significant peaks at the Fermi level, which reveals that metallic bonds are formed between metal atoms. After two Cr atoms are replaced by V atoms at Wyckoff 2b sites, there are reductions of the PDOS peaks of the Cr-d orbitals in Fe3Cr3VC3 carbide. The electron depletion of the Cr atoms can be replenished by the electrons of the V atoms. In addition, PDOS reductions of the Fe-d orbitals in Fe3Cr3VC3 carbide prove that its electron depletion is increased. Therefore, V doping can lead to the formation of stronger V—C covalent bonds and the polarities of the Cr—C and Fe—C covalent bonds are also reduced. Therefore, the mechanical properties of Fe3Cr4C3 carbides are enhanced by the improvement of the bond strength by V doping.

### 4.2. Bond fracture after tensile calculation

Schematic diagrams of the fractured chemical bonds in Fe3Cr4C3 and Fe3Cr3VC3 carbides are shown in Fig. 11, in which the tensile directions are shown by the red arrows with solid lines. Fig. 11(a) shows the tensile fracture of the chemical bonds in Fe3Cr4C3 carbide. The broken bonds of Fe3Cr4C3 carbide in the (0001) and (2110) crystal faces are Fe—C and Cr—C bonds along the tensile direction. The broken bonds of Fe3Cr4C3 carbide in the (1120) crystal face are mainly Cr—C bonds. In the fractured structure of Fe3Cr4C3 carbide in the (1121) crystal face, the Cr—C and Fe—C bonds along the tensile direction are broken. After tensile and fracture calculations, the structural distortions of the tensile calculations in the [0001] and [1121] crystal orientations are larger than those of the other crystal orientations. Fig. 11(b) shows the tensile fracture of the chemical bonds in Fe3Cr3VC3 carbide. The broken bonds of Fe3Cr3VC3 carbide in the (0001) crystal face are V—C bonds. The positions of the broken bonds in the (2110) crystal face are similar to those of Fe3Cr4C3 carbide. In Fe3Cr3VC3 carbide, the broken bonds are V—C and Fe—C bonds. Compared with Fe3Cr4C3 carbide, the number of broken bonds of Fe3Cr3VC3 carbide in the (1121) crystal face is reduced and the broken bonds are mainly V—C ones. The number of broken bonds of Fe3Cr3VC3 carbide in the (0001) and (1121) crystal faces is reduced and this can contribute to its higher tensile strength. The number of broken bonds of Fe3Cr3VC3 carbide in the (2110) and (1120) crystal faces is increased, which reveals the reason for the reduction of the tensile strength.

### 4.3. Scanning tunneling microscopy simulation of the (0001) surface

To provide a comparison between calculation and future experimental results, scanning tunneling microscopy (STM) images of the (0001) surfaces in Fe3Cr4C3 and Fe3Cr3VC3 carbides were simulated. Fig. 12 shows schematic diagrams of the (0001) surface models and STM simulation results for Fe3Cr4C3 and Fe3Cr3VC3 carbides. In Fig. 12(a), the distance between the surface layer and the subsurface II layer of the Fe3Cr4C3 (0001) surface model is 0.83 A ° . In Fig. 12(b), the distance between the surface layer and the subsurface II layer of the Fe3Cr3VC3 (0001) surface model is decreased to 0.74 Å. In Fig. 12(c), the atomic distance between the Fe atoms in a layer of Fe3Cr4C3 is 2.70 Å , that between the Cr atoms in a II layer is 4.28 Å , and that between the nearest neighbour Fe atom and Cr atom is 2.52 Å. In Fig. 12(d), the atomic distance between Fe atoms in a layer of Fe3Cr3VC3 decreases to 2.64 Å, that between the Cr atoms in a II layer increases to 4.31 Å and that between the nearest neighbour Fe atom and V atom increases to 2.57 Å. The doping V atom leads to slight lattice distortions, which lead to atomic spacing changes. In Figs. 12(e) and 12(f), STM simulation images for Fe3Cr4C3 and Fe3Cr3VC3 carbides fit well with the (0001) surface structures. It can be seen clearly that no reconstructions have occurred on either surface. Nevertheless, the corresponding positions of the Vatoms are less bright than those of the Cr atoms, which may be caused by the large electron loss of the V ions.

## 5. Conclusions

The formation enthalpy of Fe3Cr3VC3 carbide is _0.24 eV/atom, which is lower than the formation enthalpy (0.48 eV/atom) of Fe3Cr4C3 carbide. No imaginary frequency appears in the phonon spectra. The heat capacity of Fe3Cr3VC3 carbide is greater than that of Fe3Cr4C3 carbide. To sum up, Fe3Cr3VC3 carbide is relatively easier to form and is theoretically more stable than Fe3Cr4C3 carbide. Compared with Fe3Cr4C3 carbide, the tensile strength of Fe3Cr3VC3 carbide in the (0001) crystal face is increased from 44.42 to 48.46 GPa and that in the (1121) crystal face is increased from 28.99 to 34.19 GPa. The δ reductions are relatively small, in which the δ value of Fe3Cr3VC3 carbide in the (0001) crystal face is decreased from 36 to 31% and that in the (1121) crystal face is decreased from 30 to 29%. The tensile behaviours of Fe3Cr3VC3 carbide in the equivalent (2110) and (1120) crystal faces are similar and have the same bond-length changes. The bond-length change in the (0001) crystal face is the most obvious and disordered after tensile fracture. The bond-length distribution in the (1121) crystal face does not change much during the tensile process. The changes in the C—V, V—Fe and Cr—V bond lengths are relatively small compared with other chemical bonds, which can contribute to the improvement in strength. V atoms can provide more electrons than Cr atoms and can thus reduce the electron loss of the neighbouring Fe and Cr atoms, which can contribute to an improvement in the strength of metallic and covalent bonds. The electron redistribution and the formation of stronger chemical bonds caused by V doping is the reason for the tensile property improvement of Fe3Cr3VC3 carbide.


### Funding information

The following funding is acknowledged: National Natural Science Foundation of China (grant No. 51771167 to QY); EU H2020 Marie Skłodowska-Curie project ‘i-Weld’ (grant No. 823786 to XR).


### References


Becke, A. D. & Edgecombe, K. E. (1990). J. Chem. Phys. 92, 5397–5403.
Bedolla-Jacuinde, A. (2001). Int. J. Cast Met. Res. 13, 343–361.
Blo¨ chl, P. E. (1994). Phys. Rev. B, 50, 17953–17979.
Buchanan, V. E., Shipway, P. H. & McCartney, D. G. (2007). Wear, 263, 99–110.

Chong, X. Y., Hu, M. Y., Wu, P., Shan, Q., Jiang, Y. H., Li, Z. L. & Feng, J. (2019). Acta Mater. 169, 193–208.
Fan, Q., Li, D., Li, J. &Wang, C. (2020). J. Alloys Compd. 829, 154483.
Gao, X., Jiang, Y., Zhou, R. & Feng, J. (2014). J. Alloys Compd. 587, 819–826.
Guo, L., Tang, Y., Cui, J., Li, J., Yang, J. R. & Li, D. Y. (2021). Scr. Mater. 190, 168–173.
Kang, J., Li, J., Wu, F., Li, S. S. & Xia, J. B. (2011). J. Phys. Chem. C, 115, 20466–20470.
Khvan, A. V., Hallstedt, B. & Broeckmann, C. (2014). Calphad, 46, 24–33.
Kresse, G. & Furthmu¨ ller, J. (1996). Phys. Rev. B, 54, 11169–11186.
Li, D., Liu, L., Zhang, Y., Ye, C., Ren, X., Yang, Y. & Yang, Q. (2009). Mater. Des. 30, 340–345.
Li, N., Huang, S., Zhang, G., Qin, R., Liu, W., Xiong, H., Shi, G. &Blackburn, J. (2019). J. Mater. Sci. Technol. 35, 242–269.
Li, Y., Hao, J., Liu, H., Lu, S. & Tse, J. S. (2015). Phys. Rev. Lett. 115, 105502.
Liao, M., Liu, Y., Cui, P., Qu, N., Zhou, F., Yang, D., Han, T., Lai, Z. & Zhu, J. (2020). Comput. Mater. Sci. 172, 109289.
Liao, M., Liu, Y., Min, L., Lai, Z., Han, T., Yang, D. & Zhu, J. (2018). Intermetallics, 101, 152–164.
Liao, N., Zhang, M., Zheng, B. & Xue, W. (2020). Mater. Today, 18, 100434.
Lu, W., Yan, B., Li, Y. & Tang, R. (2008). J. Alloys Compd. 454, L10–L13.
Lu, Y., Wang, Y., Wang, Y., Gao, M., Chen, Y. & Chen, Z. (2021). J. Mater. Sci. Technol. 70, 83–90.
Miao, Y., Bao, H., Fan,W. & Ma, F. (2020). J. Phys. Chem. Solids, 142, 109459.
Perdew, J. P., Burke, K. & Ernzerhof, M. (1996). Phys. Rev. Lett. 77, 3865–3868.
Petit, A. T. & Dulong, P. L. (1819). Ann. Chim. Phys. 10, 395–413.
Rahman, N., Capuano, L., Cabeza, S., Feinaeugle, M., Garcia-Junceda, A., de Rooij, M. B., Matthews, D. T. A., Walmag, G.,Gibson, I. & Ro¨ mer, G. R. B. E. (2019). Addit. Manuf. 30, 100838.
Rogl, G., Sauerschnig, P., Rykavets, Z., Romaka, V., Heinrich, P., Hinterleitner, B., Grytsiv, A., Bauer, E. & Rogl, P. (2017). Acta Mater. 131, 336–348.
Roundy, D., Krenn, C. R., Cohen, M. L. & Morris, J. W. (1999). Phys. Rev. Lett. 82, 2713–2716.
Wang, J., Guo, W., Sun, H., Li, H., Gou, H. & Zhang, J. (2016). Mater. Sci. Eng. A, 662, 88–94.
Wei, W., Xu, K., Liao, N. & Xue, W. (2020). Mater. Today, 20, 100773.
Wiengmoon, A., Chairuangsri, T., Brown, A., Brydson, R., Edmonds, D. V. & Pearce, J. T. H. (2005). Acta Mater. 53, 4143–4154.
Xie, J. Y., Chen, N. X., Shen, J., Teng, L. & Seetharaman, S. (2005). Acta Mater. 53, 2727–2732.
Yılmaz, O. & Turhan, H. (2001). Compos. Sci. Technol. 61, 2349–2359.
Yin, B., Maresca, F. & Curtin, W. A. (2020). Acta Mater. 188, 486–491.
Zhang, M., Liu, H., Li, Q., Gao, B., Wang, Y., Li, H., Chen, C. & Ma, Y. (2015). Phys. Rev. Lett. 114, 015502.
Zhang, M., Lu, M., Du, Y., Gao, L., Lu, C. & Liu, H. (2014). J. Chem. Phys. 140, 174505.
Zhang, P., Zhou, Y., Yang, J., Li, D., Ren, X., Yang, Y. & Yang, Q. (2013). J. Alloys Compd. 560, 49–53.
Zhi, X., Xing, J., Gao, Y., Fu, H., Peng, J. & Xiao, B. (2008). Mater. Sci. Eng. A, 487, 171–179.

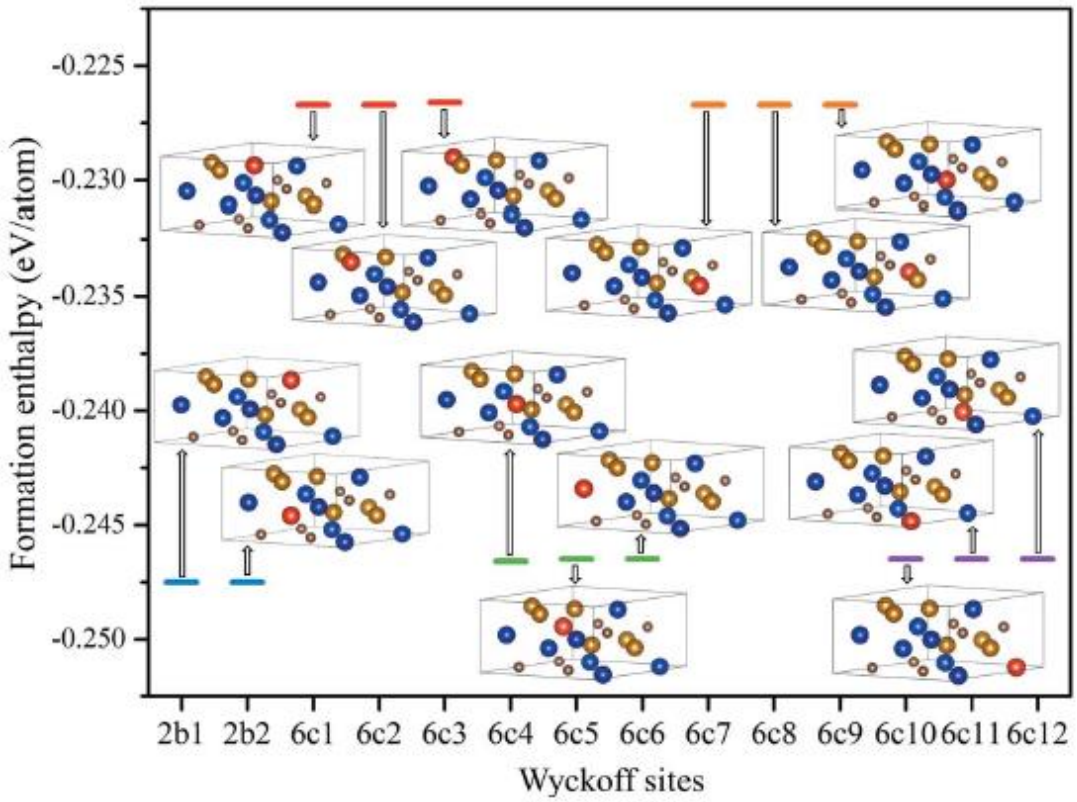


*Figure 1* Schematic structures and formation enthalpy of Fe3Cr4C3 and FexCr6.5–xV0.5C3 carbides.

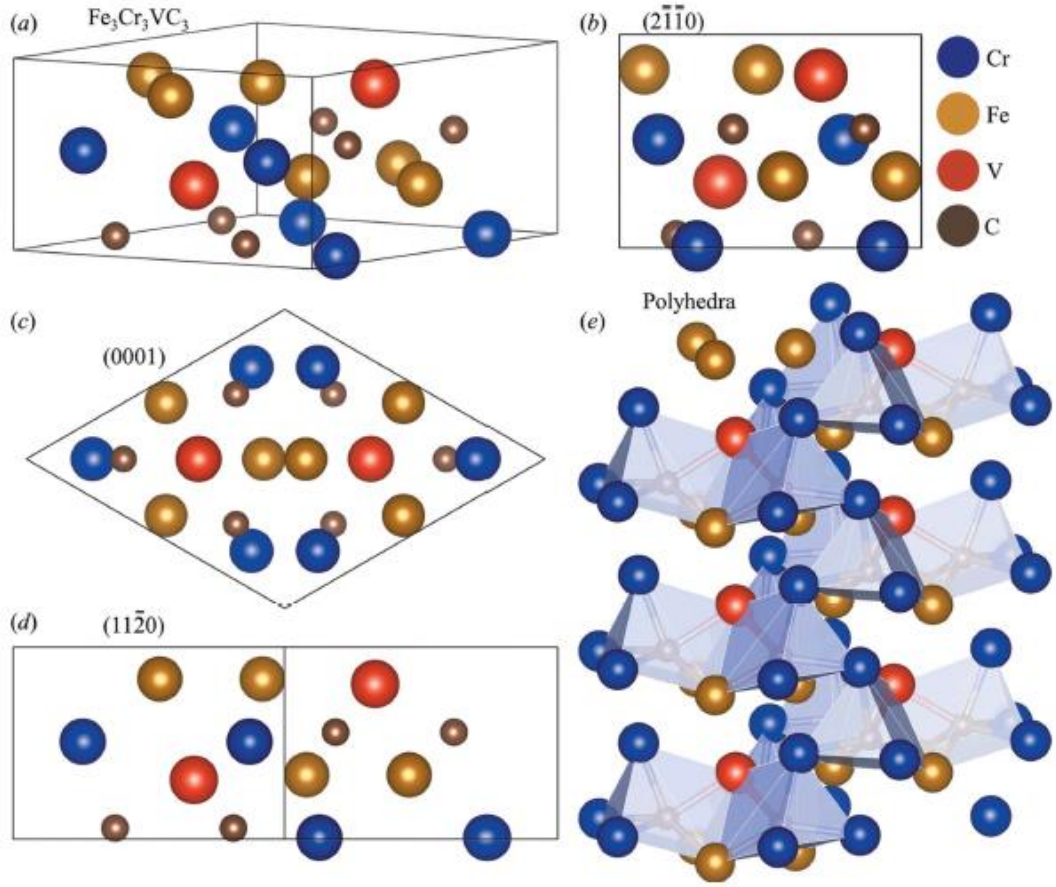


*Figure 2* Views of (a) the unit cell, (b) the (2110) face, (c) the (0001) face, (d) the (1120) face and (e) the polyhedral structure of Fe3Cr3VC3 carbide

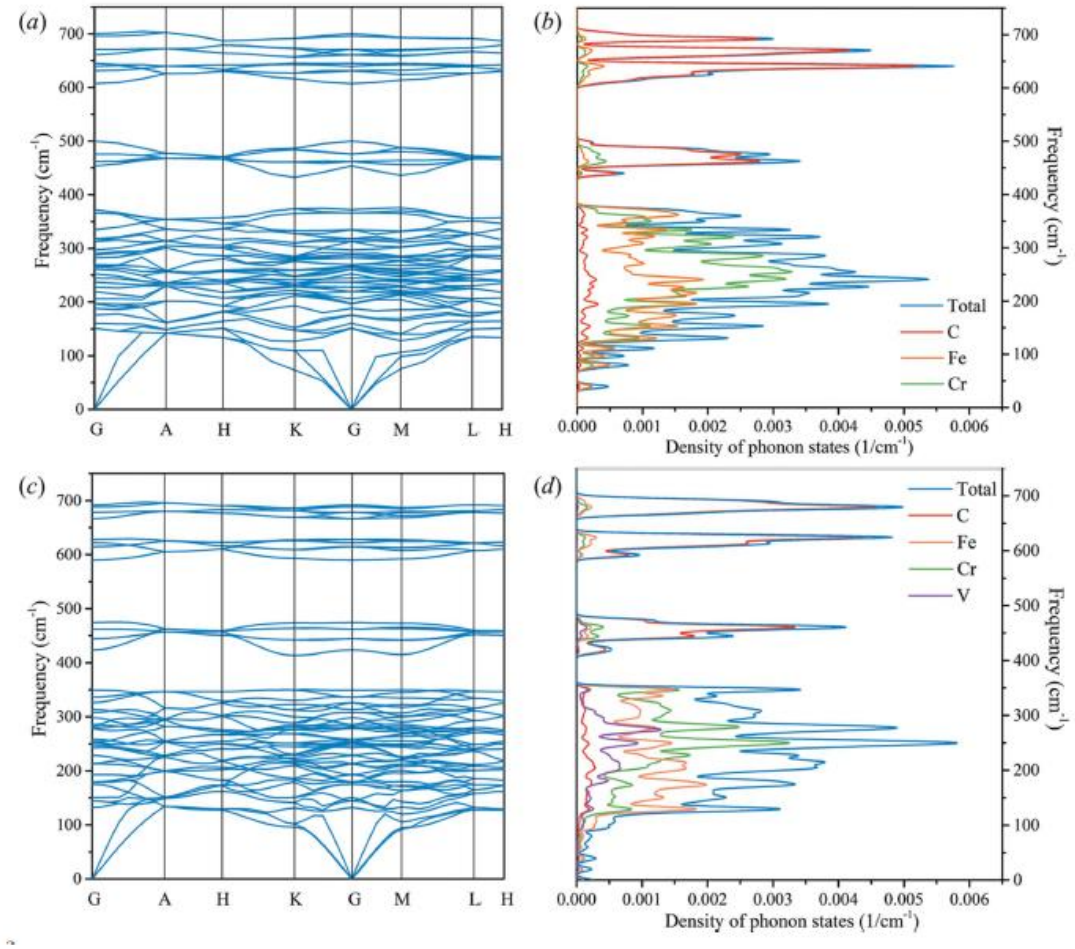


*Figure 3* (a) Phonon dispersion spectra of Fe3Cr4C3 carbide and (b) its phonon density of states (PHDOS). (c) Phonon dispersion spectra of Fe3Cr3VC3 carbide and (d) its PHDOS.

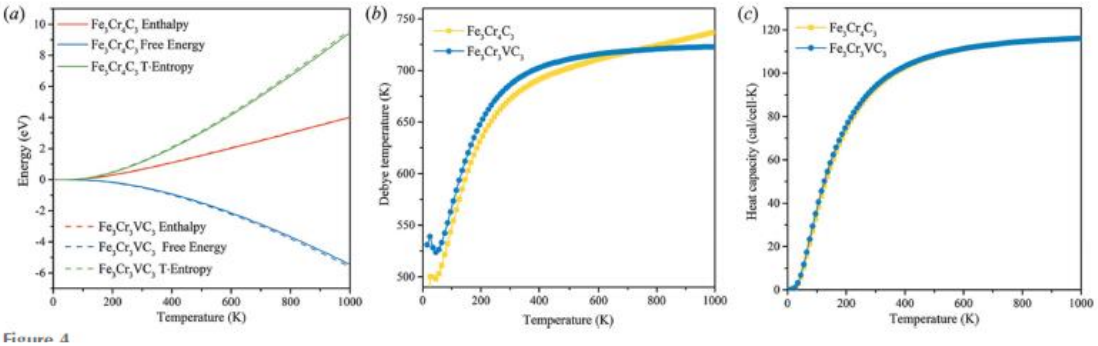


*Figure 4* Energy changes, (b) Debye temperature and (c) heat capacity curves of Fe3Cr4C3 and Fe3Cr3VC3 carbides.

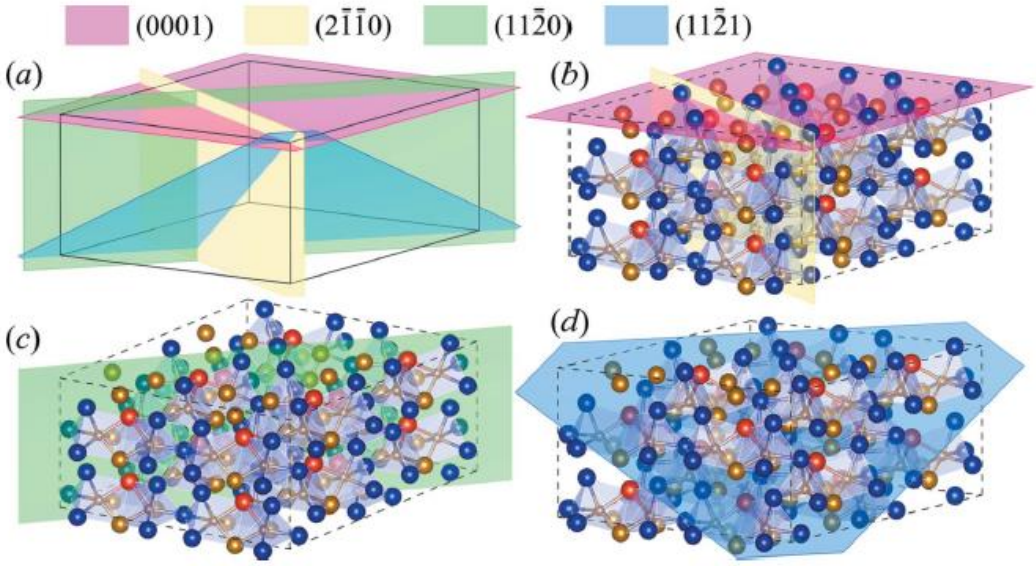


*Figure 5* The locations of (a) the four crystal faces, (b) the (0001) and (2110) planes, (c) the (1120) plane and (d) the (1121) plane.

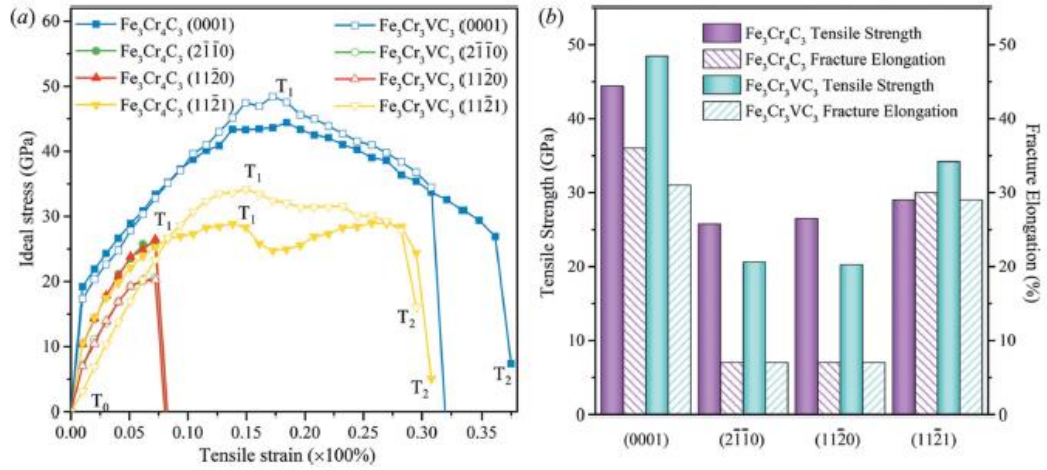


*Figure 6* Tensile stress-strain curves of Fe3Cr4C3 and Fe3Cr3VC3 carbides, and (b) histogram of tensile strength and fracture elongation.

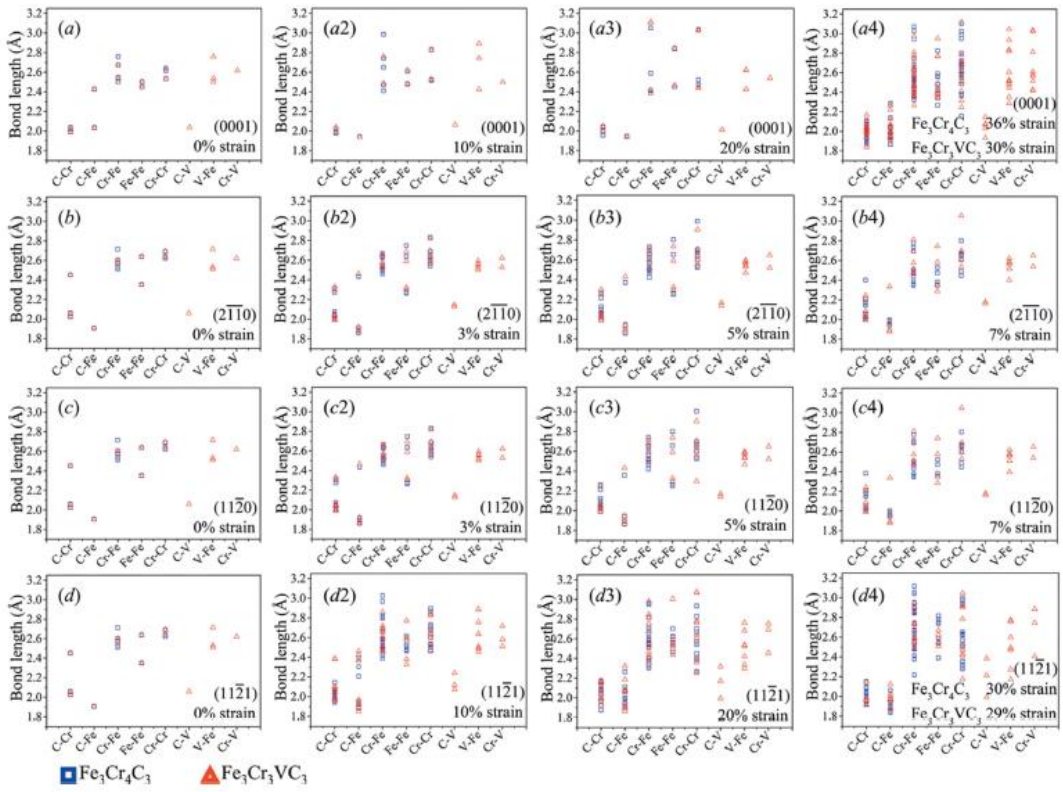


*Figure 7* Bond-length distribution in the (a) (0001), (b) (2110), (c) (1120) and (d) (1121) crystal faces of Fe3Cr4C3 and Fe3Cr3VC3 carbides. Parts (ai), (bi), (ci) and (di) represent different crystal faces with various strains, where i = 2, 3 and 4.

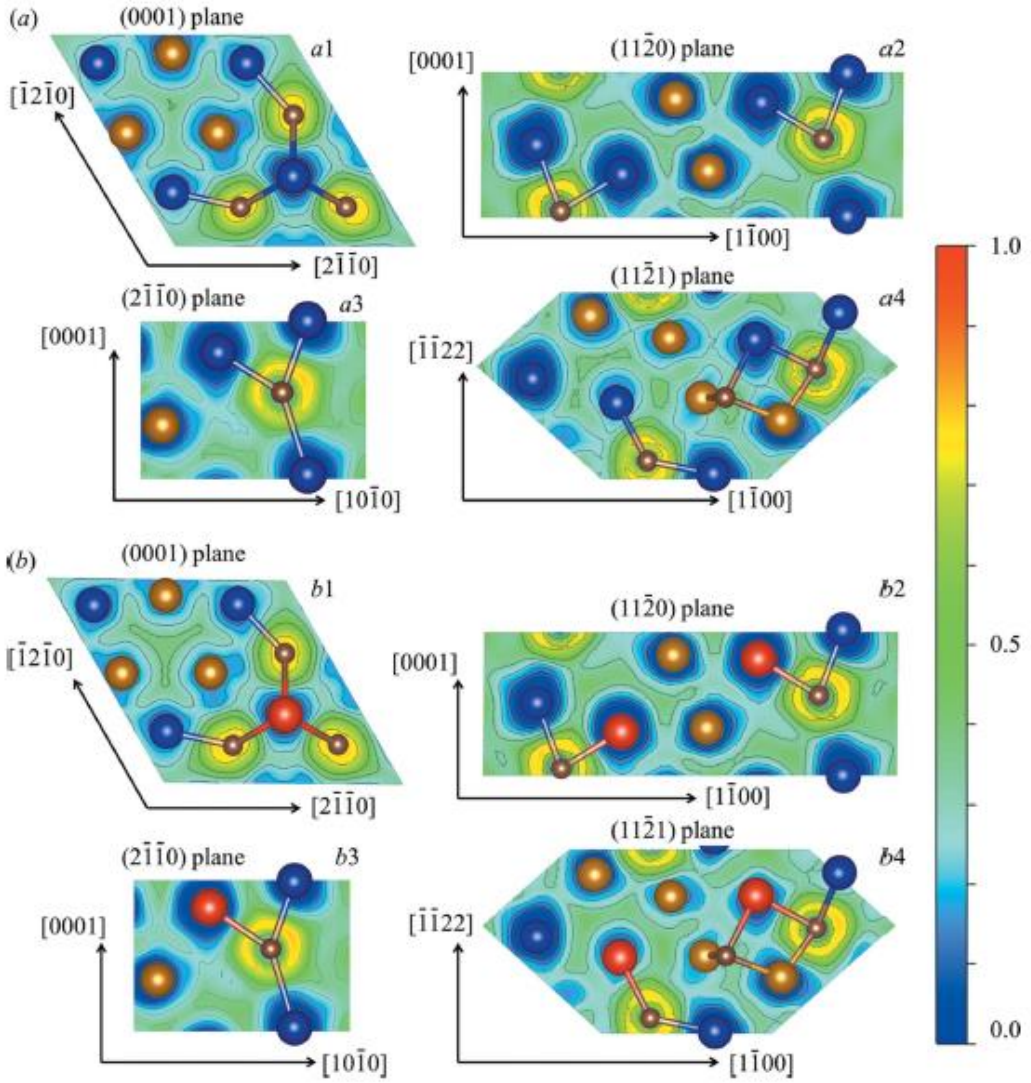


*Figure 8* ELF planar projections of (a) Fe3Cr4C3 and (b) Fe3Cr3VC3 carbides in the (0001), (2110), (1120) and (1121) crystal faces.

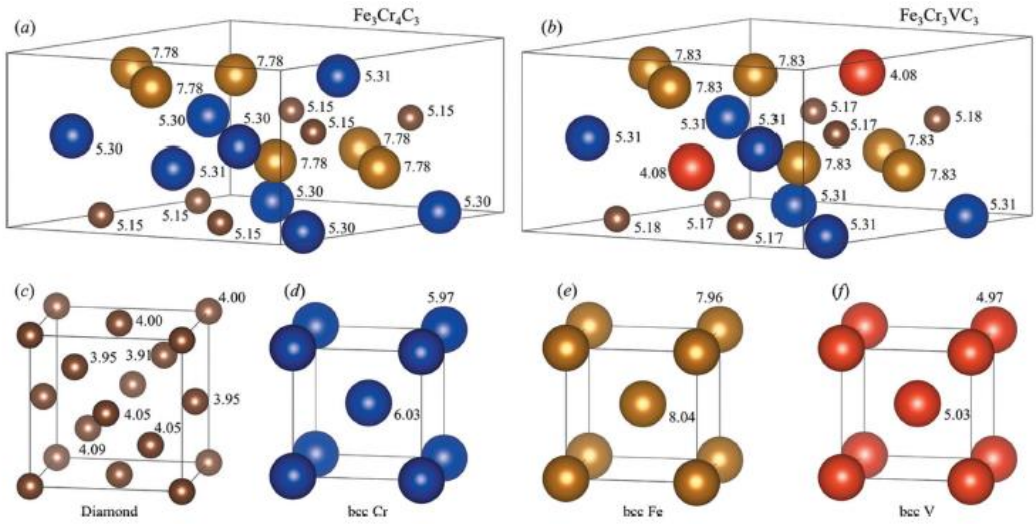


*Figure 9* Bader charges of atoms in (a) Fe3Cr4C3, (b) Fe3Cr3VC3, (c) diamond, (d) bcc C, (e) bcc Fe and (f) bcc V crystal models.

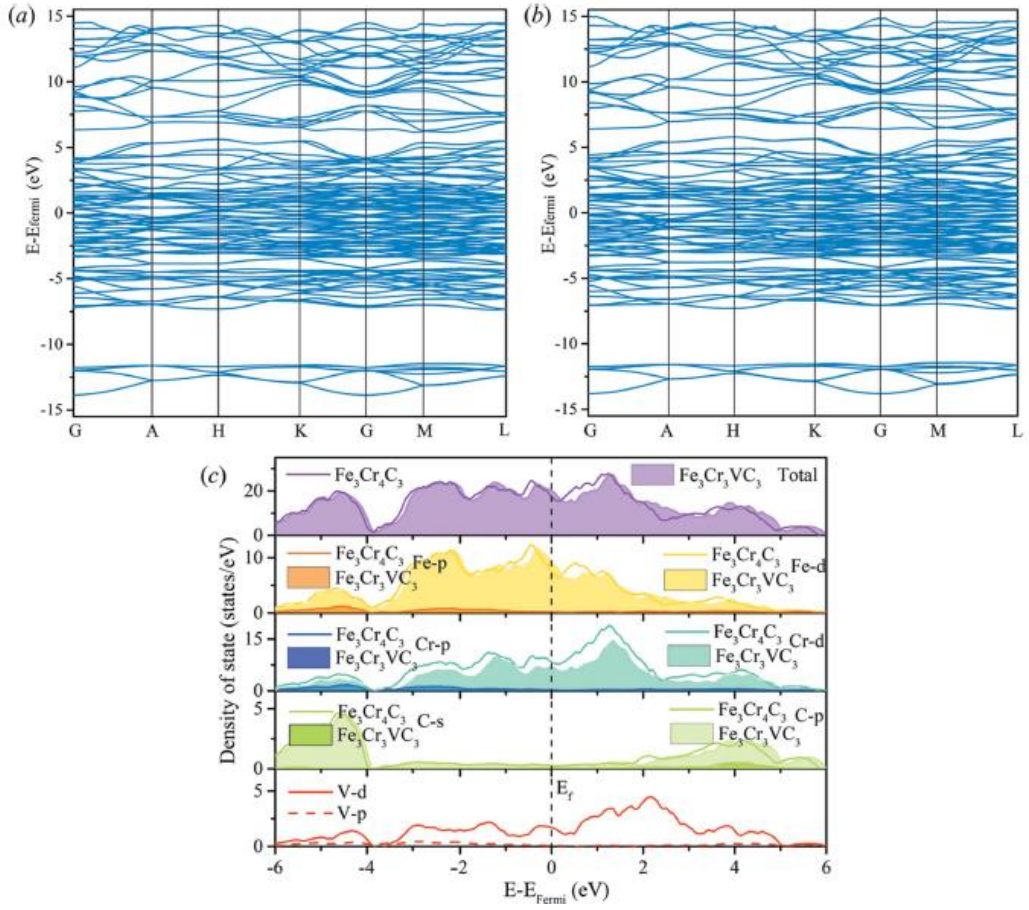


*Figure 10* Band structures of (a) Fe3Cr4C3, (b) Fe3Cr3VC3 carbides and (c) their density of states.

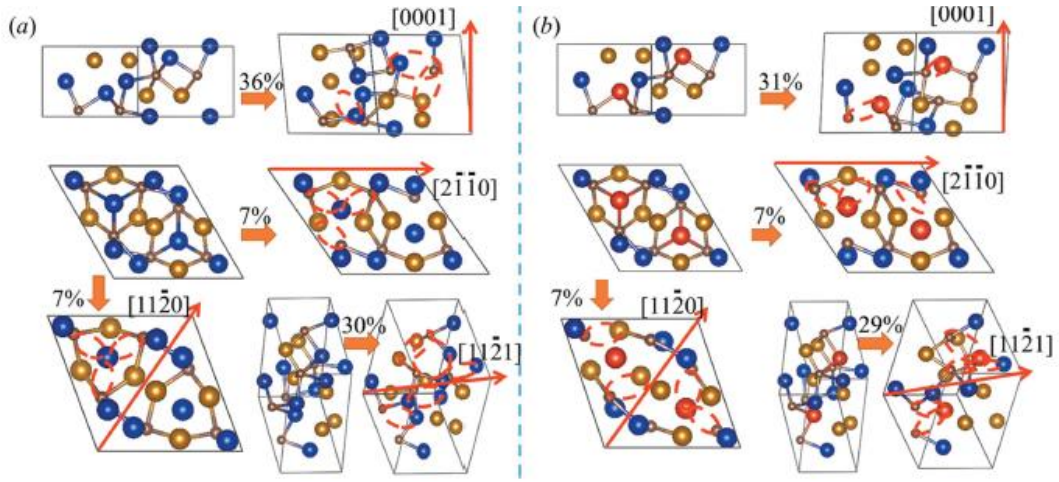


*Figure 11* Schematic diagrams of bond fracture in (a) Fe3Cr4C3 and (b) Fe3Cr3VC3 carbides.

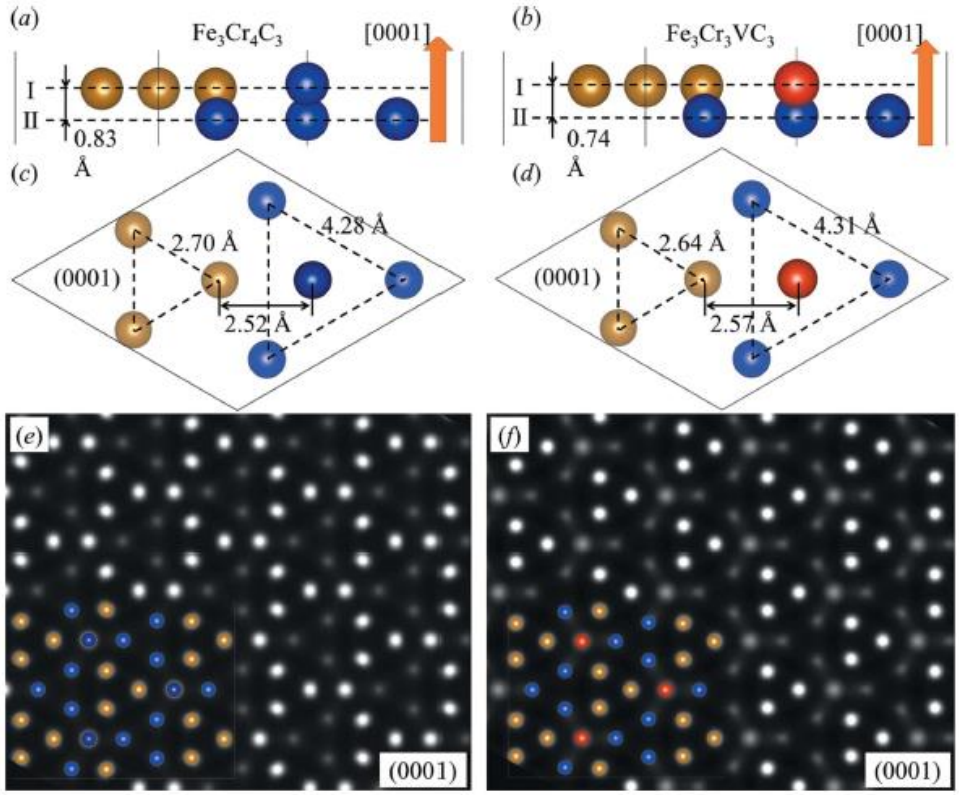


*Figure 12* (1010) views of (a) Fe3Cr4C3 and (b) Fe3Cr3VC3 (0001) surface models, and (0001) views of (c) Fe3Cr4C3 and (d) Fe3Cr3VC3 (0001) surface models. STM simulation images of (0001) surfaces in (e) Fe3Cr4C3 and (f) Fe3Cr3VC3 carbides.